scientific reports

Check for updates

OPEN

Potential geological risks from mud diatremes in the orogen regime of Southwestern Taiwan

Hung-Yu Wu[1], Hou-Chun Liu[2]✉, Li-Cheng Kao[1], Kuo-En Ching[3], Chien-Chih Chen[4], Chen-Feng You[2], Te-Cheng Yi[2], Yan-Hong Chen[2], Bo-Lin Wu[5] & Chun-Jung Chen[6]

In orogenic regions, faults from plate collisions are the main cause of earthquakes. Recent studies have found that underground mudstone structures and intrusions can accompany fault development, causing surface deformation and geological hazards. In southwestern Taiwan, geodetic evidence has detected underground mudstone structures, but their mechanisms of influence remain unclear. This study conducted cores drilling at a hotspot showing positive gravity anomaly. Multi-disciplinary analyses confirmed that sediments came from mudstone at least 3 km in depth. The observed compression validated surface-reaching mudstone intrusions. Electrical resistivity tomography revealed scattered mud intrusions cause localized uplift, potentially damaging structures. This suggests the large mud intrusion/mud diapir extends to shallow depth below the surface, with fractures acting as conduits to the ground (mud diatreme). Mud structures have been found in both collisional and extensional regions, suggesting they influence fault development and surface deformation widely, raising safety concerns in urban due to these geological risks.

Scientific Reports (R1: Jan 2025).

Introduction

In tectonic active areas, such as cities situated in orogenic regimes, earthquakes often cause substantial damage on buildings and pose significant risks to residential safety. This is primarily due to earthquake-induced ground shaking, resonance, soil liquefaction, and surface ruptures[1–8], which often compromise load-bearing structures such as foundations, beams, and walls. Consequently, building damage, particularly cracks and deformations, is commonly attributed to earthquake disasters.

In the orogenic active SW Taiwan, damage has been found in at least 16 public buildings and private residences, including high schools, universities, hospitals, and transportation facilities[9] (Fig. 1). While initially it was attributed to earthquakes, further investigation revealed that these buildings were not located along fault lines (Fig. 2), suggesting that faults and earthquakes might not have been the primary causes. Besides, according to the earthquake catalog since 1990, there has been almost no seismic activity at depths shallower than 12 km[10], making this region one of aseismic zones in Taiwan. Instead, the damaged buildings are widely distributed over the Tainan and Chungchou anticlines (Folds A and C in Fig. 2), which are mud-based structures formed under compressive conditions[11]. The upward development of the mudstone structure is attributed to the entrapment of large volumes of seawater during the rapid mud deposition. Subsequently, within the foreland basin formed under tectonic compression[12], overpressured fluids released along fractures that developed at the crest of the mud-cored anticline due to horizontal compressive stress[13]. According to earlier monitoring, geodetic data indicates a surface deformation rate of up to 10 mm yr^{-1} in this area[14,15]. This deformation can lead to nonuniform surface changes, causing fractures between primary building structures and the ground surface, or within the main structures. While this gradual deformation may not cause immediate and extensive damage like earthquakes or soil liquefaction, its slow but continuous progression raises ongoing concerns about the structural integrity of buildings, bridges, and railways, thereby impacting community safety.

The positive residual gravity anomaly supports a hypothesis regarding the underlying mud structure and further suggests that the surface deformation is likely due to mud uplift penetrating the overlying sedimentary

[1]Department of Resources Engineering, National Cheng Kung University, No.1, University Road, East District, Tainan City 70101, Taiwan. [2]Department of Earth Sciences, National Cheng Kung University, Tainan City 70101, Taiwan. [3]Department of Geomatics, National Cheng Kung University, Tainan City 70101, Taiwan. [4]Department of Earth Sciences, Graduate Institute of Applied Geology and Earthquake-Disaster and Risk Evaluation and Management Center, National Central University, Taoyuan 320317, Taiwan. [5]Archaeo Cultures CO., LTD, Tainan City 744093, Taiwan. [6]National Museum of Natural Science, Taichung City 404023, Taiwan. ✉email: liuhouchun@gs.ncku.edu.tw

Fig. 1. The damaged buildings and infrastructures due to land surface deformation. (**a**,**b**) Uniform surface deformation leads to buildings separating from surrounding ground facilities, causing damage that is very common in SW Taiwan. However, (**c**,**d**) in regions with high deformation rates, severe land surface deformation can significantly damage the structures of buildings and infrastructure (e.g., transmission towers), raising safety concerns.

layers[9,11,16], specifically the mud diapirs[17] (Fig. 3a). Offshore mud volcanoes in this area have previously been confirmed to be associated with mud diapiric intrusions in the upper Kaoping Slope[18,19]. The onshore mud structures are thought to be extensions of these offshore mud diapirs[18–20]. Currently, there are two active anticlines with an average uplift rate of 10–12 mm yr^{-1} driving surface deformation[14,15,21]. Despite this, numerous discrepancies between this diapir model and observations that need to be clarified. On one hand, based on geological investigations in this area, these mud diapirs are reported not to reach the ground surface, remaining approximately 30–50 m below the surface in Tainan urban[9]. On the other hand, up to one-fourth of the damaged buildings are situated in the negative residual anomaly zone (Fig. 2), suggesting that these structures are not directly affected by the intrusions of mud diapirs. Additionally, the extent of land deformation varies significantly, spanning from a few meters to several hundred meters[9,22]. Hence, these findings suggest that a broad-scale mud uplifting movement alone cannot fully account for the observed damages. A new model, capable of explaining the multiple isolated hotspots and laterally extended effects, is necessary.

Mud diatremes (Fig. 3b), typically located at the boundaries of plate convergence and developed in connection with mud diapirs, are thought to act as conduits containing sediment undergoing fluidization[22]. The conduits of mud diatremes exhibit distinct anisotropic scaly fabrics, forming within the marginal shear zone of diapirs during the deformation and compaction of the mud matrix[22]. Since mud diapirs typically grow in association with active faults[23], the scaly fabrics observed in outcrops are often interpreted as high-angle reverse fault zones[22]. Hence, it is likely that the mud diapiric intrusions extend very close to the shallow subsurface, with the ensuing development of mud diatremes being the primary cause leading to surface deformation and direct damage to buildings.

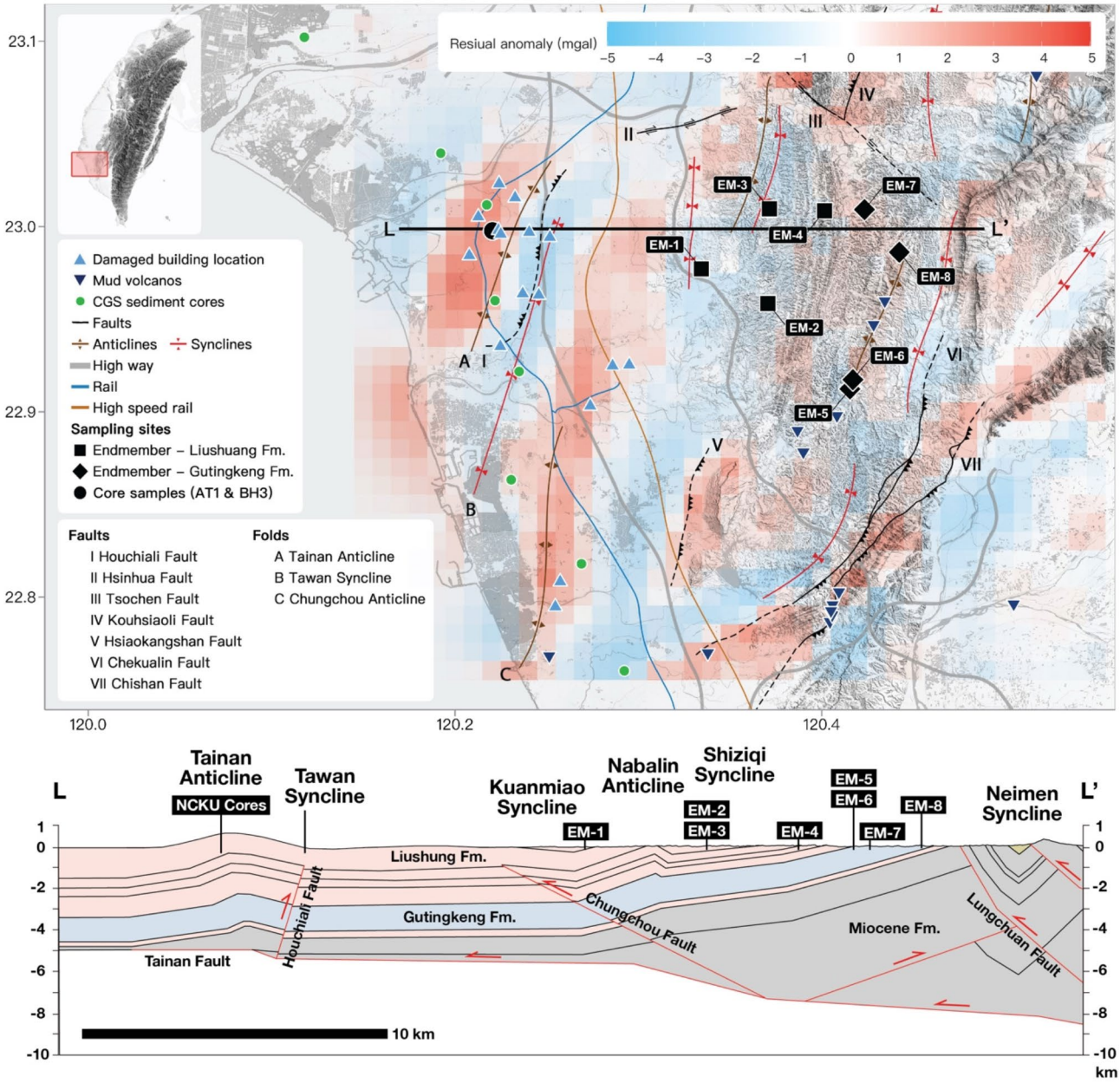

Fig. 2. Regional geology and surface residual anomaly of the study area. The geological map was redrawn based on the open data from Geological Survey and Mining Management Agency, MOEA, Taiwan. The data of surface anomaly was from Lo et al. (2023)[16]. The reported damaged public buildings (up-pointing triangle) and mud volcanoes (down-pointing triangle) are located near the positive residual anomaly zone. The samples in this study are represented by a black-colored circle symbol for sediment core and square and diamond symbols for endmember sediments.

To validate this hypothesis, we have conducted drilling cores at the focal point of the positive residual gravity anomaly region. This involved a 100-meter borehole at the surface uplift hotspot and another 20-meter borehole in the nearby location as a comparative reference. If the mechanism behind surface land deformation is the mud diatreme, the sediment within the 100-meter borehole (AT1) would likely originate from the deep mud layer and undergo compression. In contrast, the reference site, namely the 20-meter borehole (BH3), would exhibit a conventional depositional sequence rather than such compression patterns. Here, we determined the porosity of the drilled cores to confirm the occurrence of compression processes in the sediment. We employed isotope geochemical and synchronous X-ray absorption techniques to trace the sediment sources. The collective multi-disciplinary evidence meets the crucial criteria for the mud diatreme phenomenon, marking the first direct evidence of surface damage caused by underground mud-base deformation in orogen regimes.

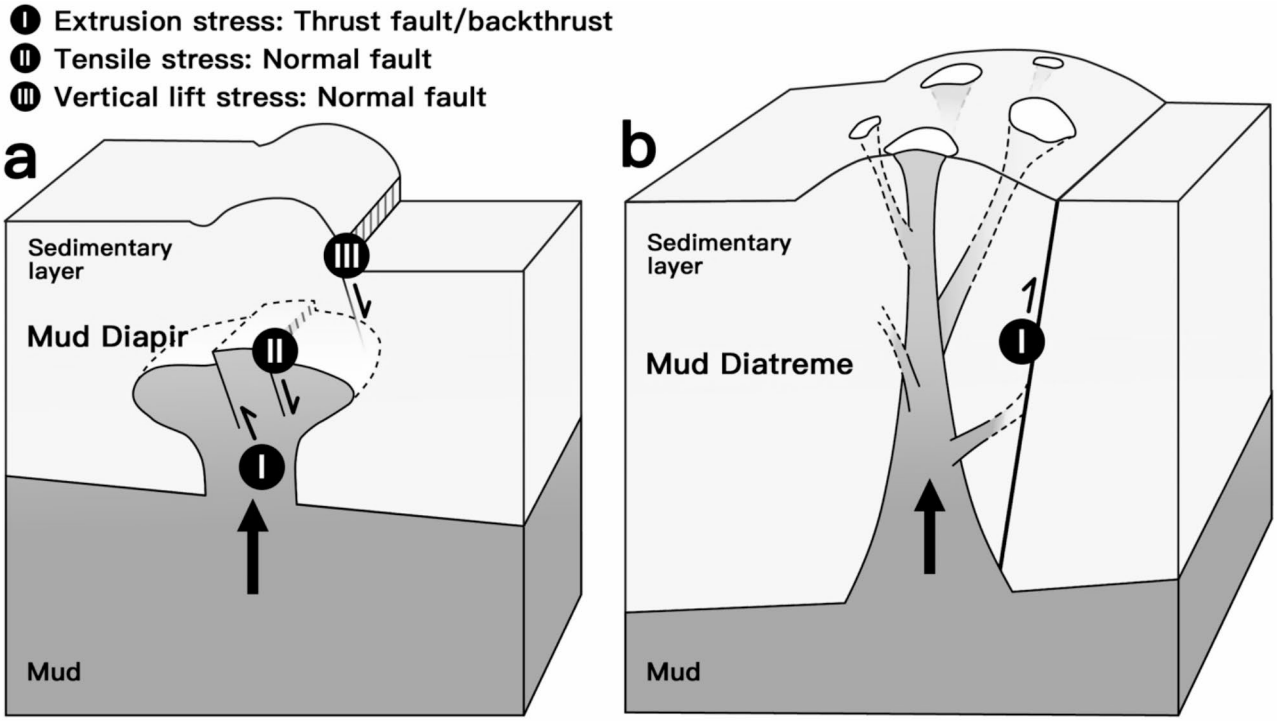

Fig. 3. Conceptual models of mud diapir and mud diatreme and associated features. (**a**) Mud Diapirs (modified from Pérez-Belzuz et al. (1997)[72]) typically form due to mud ascending through overlying sedimentary layers; (**b**) mud diatremes (modified from Brown (1990)[22]) usually result from the explosive release of high-pressure, fluidized mud sediments into overlying layers.

Methods

Studying materials

This project included one borehole (AT1), drilled at the hotspot of the active mud regime to a depth of 100 m, and another borehole (BH3), located 65 m away from AT1 and drilled to a depth of 20 m, for reference. Due to drilling permit reasons, those drilling sites are located within the campus of National Cheng Kung University (NCKU), specifically at the location marked as "NCKU Cores" in Fig. 2. Despite the two core-drilling sites being in close proximity, visual inspections reveal a clear difference at the ground surface: the AT1 site exhibits noticeable uplift, while no such elevation is apparent at the BH3 site. The borehole samples were subjected to a series of geophysical and geochemical analyses, including grain size distribution, porosity, X-ray diffraction for mineralogical identification, C-14 dating, synchrotron-based XAS at Fe K-edge analysis, and chemical and Nd isotopic determinations. To identify the sediment sources for the boreholes, we collected reference sediments from the eastern side of the Tainan Tableland, where the stratigraphic units are well-defined. These samples represent the standard depositional sequence: the surface Holocene deposits (EM1), Liushuang Formation (EM2–4), and Gutingkeng Formation (EM5–8). Of these, the Holocene and Liushuang Formations make up the near-surface strata in our study area, whereas the Gutingkeng Formation is found at depths of at least three kilometers below the surface. Those samples underwent analysis for their geophysical and isotopic properties and were utilized as endmembers for identifying sediment provenance. The detailed information and the sampling sites for these specimens are given in Fig. 2 and Supplementary Table S1.

Electrical resistivity tomography

Electrical resistivity tomography (ERT) is a non-destructive survey method that uses a direct current to create an artificial current source. By measuring the potential difference between electrodes, ERT assesses subsurface resistivity at various depths. Numerical inversion and interpolation of the data produce a profile of the true subsurface resistivity[24]. The electrode configuration and switching rules in ERT surveys are known as electrode arrays. This study uses the CPP array[25], where each electrode is fixed as either a current or potential electrode. The array features one current electrode (C) and two potential electrodes (P) arranged alternately. ERT was conducted in our study area spanning approximately 400 m in length and reaching nearly 100 m in depth (Fig. 4). During measurements, two C electrodes discharge while a reference potential electrode measures all P electrodes, allowing for multi-channel measurements. This approach is faster and generates more data points compared to traditional methods. Additionally, it collects data from other electrode arrays for extraction and comparison.

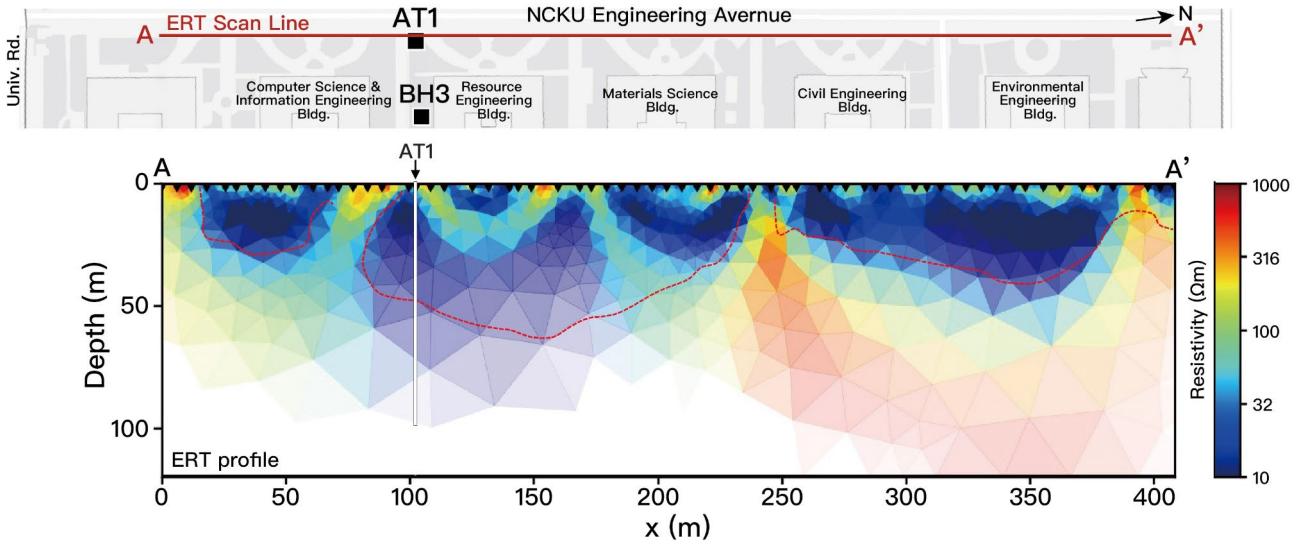

Fig. 4. An ERT profile scanned in areas with positive residual anomalies. A 400-meter-long ERT survey was conducted along Engineering Avenue on the NCKU campus. The profile revealed several low-resistivity zones extending from the surface to deep underground, indicating mud intrusion from depth to shallower levels. We drilled a 100-meter borehole (AT1) at the hotspot of the low-resistivity zones and a 20-meter borehole (BH3) some distance away from core AT1.

Sediment grain size and porosity for the boreholes

Particle grain size distributions in the boreholes were analyzed using a PSA 1190 laser particle size analyzer (Anton Paar Company, Austria), covering a size range from 0.04 μm to 2500 μm. Sediment samples, approximately 1–3 g in dry weight, were collected from each 10 cm-section within every 1 m interval. Organic matter was removed using 30% hydrogen peroxide, followed by grain size analyses on the samples.

Sediment core porosity was determined through Geotek core descriptions and multi-sensor core log (MSCL) conducted at the Marine Core Repository and Laboratory of the Taiwan Ocean Research Institute (TORI). The cores underwent gamma ray attenuation scanning at a 0.5-cm interval. Subsequently, fractional porosity for the boreholes was computed based on the gamma density, sediment average density (2.650 g cc^{-1}), and water/air density (1.026 g cc^{-1})[26]. Therefore, the fractional porosity is directly correlated with gamma density.

Radiocarbon dating

Radiocarbon dating was conducted on three different material types: organic sediment (9 samples), shells (4 samples), and charred material (1 sample). The samples underwent pre-treatment processes, which included HCl acid wash, acid etching, or alkali acid dissolution, tailored to the specific sample types. Subsequently, these samples were analyzed using accelerator mass spectrometry at the Beta Analytical Testing Laboratory (United States). The conventional radiocarbon ages have been corrected for the fractionation effects, with the $\delta^{13}C$ correction determined separately through an isotope ratio mass spectrometer. The age calibration was performed using the database INTCAL20[27].

X-ray diffraction analyses

The sediment samples underwent pulverization into fine powders with a particle size of less than 0.25 mm. One gram of the powdered sample was dedicated to X-ray diffraction (XRD) analysis. These XRD analyses were performed at the National Museum of Natural Science, Taiwan, using a Shimadzu XRD-6000 diffractometer equipped with copper tube target radiation, operating at 35.0 kV and 25.0 mA. The samples were scanned within the range of 2° to 80° (2θ) at a scanning rate of 1° per minute. To quantify the relative abundance of major minerals, the QUALX2 software with the POW_COD database was employed.

Synchrotron-based X-ray absorption spectroscopy (XAS)

The Fe K-edge XAS spectra were collected in fluorescence mode and were recorded at beamline 12B2 in Spring-8 of the Taiwan beamline at the National Synchrotron Radiation Research Center (NSRRC), Japan. The electron storage ring operated at 8.0 GeV with a constant current of approximately 100 mA. The bending magnet BL 12B2, equipped with a Si (111) double crystal monochromator, provided a photon beam with an energy range of 5 keV to 70 keV. The incident photon energy was calibrated using Fe foil. Spectral processing and data analysis were conducted using the Demeter software package[28]. Linear combination fitting (LCF) was used to analyze sample spectra and to extract quantitative information regarding the oxidation state of the elements of interest.

Elemental and Nd isotopic determinations

One hundred mg of the dry powder (sediments from boreholes AT1, BH3, and endmembers) underwent digestion utilizing a concentrated mixture of HF and HNO_3 in a 1:2 volume ratio, heated to 120 °C. After full digestion, the samples were carefully dried and subsequently heated using concentrated HCl to eliminate CaF_2 precipitates. Finally, the samples were dried again and re-dissolved in a 0.3 M HNO_3 solution.

Major elements (Na, Mg, Ca, and K) and the trace element of Nd of samples were measured by inductively coupled plasma optical emission spectrometer (ARCOS, Spectro, Germany) at the Department of Earth Sciences, National Cheng Kung University (NCKU). The samples underwent dilution using a 5% HNO_3 acid at a dilution factor of 100. For precise concentration quantification, matrix-matched standards prepared from high-purity single-element solutions (High-Purity Standards, United States) were employed. A basalt standard (BHVO-2) was further used to ensure the quality of the determinations. The analytical relative standard deviations (RSD) were generally better than ± 3%.

Matrix separation and Nd purification were performed using a two-stage column procedure[29]. The first column with AG50W-X8 resin (200–400 µm, Eichrom, United States) was used to separate the rare earth elements (REEs) from the sample matrix; subsequently, the second column with Ln Resin (50–100 µm, Eichrom, United States) was further employed to separate Nd from the other REEs, particular the interference element of Sm. The Nd recovery all exceeded 90%; the total procedure blank was minimal, measuring less than 20 pg, which is negligible considering the 50 ng of Nd utilized in the separation experiments.

The measurements of Nd isotopic ratios were conducted using a multi-collector inductively coupled plasma mass spectrometer (Neptune, Thermo-Fisher Scientific, Germany) at NCKU, which was equipped with a high-efficiency dry interface pump to enhance signal stability and sensitivity. Sample solutions containing 10 ng g^{-1} Nd were used for the $^{143}Nd/^{144}Nd$ isotopic determinations. To account for isobaric interference from ^{144}Sm on ^{144}Nd, we monitored ^{147}Sm ion-beam and employed a $^{147}Sm/^{144}Sm$ ratio of 4.838710 for correction. An internal normalization was applied to correct the mass bias effect on the measured $^{143}Nd/^{144}Nd$ ratios by using a constant $^{146}Nd/^{144}Nd$ ratio of 0.7219. The operating conditions were fine-tuned to optimize ion beam stability. Data were collected for 60 cycles per measurement, each with an acquisition time of 4.196 s and idle time of 3.0 s. Finally, the $^{143}Nd/^{144}Nd$ ratios of the samples were normalized to the chondritic uniform reservoir (CHUR) ratio of 0.512638, as proposed by Jacobsen and Wasserburg (1980)[30] and expressed using the ε-notation:

$$\varepsilon_{Nd} = \left[\frac{\left(^{143}Nd/^{144}Nd\right)_{sample}}{\left(^{143}Nd/^{144}Nd\right)_{CHUR}} - 1 \right] \times 10{,}000 \quad (1)$$

The internal precision (2SE) of the measurements typically ranged from ± 0.000005 to ± 0.000027. Specifically, for BHVO-2 $^{143}Nd/^{144}Nd$, the reproducibility was determined to be 0.51298 ± 0.00002 (with εNd = 6.7 ± 0.4, 2SD, $n = 4$)[31–34].

Results and discussion

Underground structure revealed by electrical resistivity tomography

The ERT results (Fig. 4) shed light on the geophysical properties of the subsurface formations. Several low-resistivity zones were found above a depth of 50 m, representing extensive, recently deposited marine sediments that are widespread throughout the study region[9]. Notably, a low-resistivity zone was identified between 80 and 160 m along the survey line (x-axis), extending down to a depth of 100 m. This downward-extending geophysical feature potentially imply the presence of low-resistivity materials from deep underground, such as mud. Based on the ERT analyses, the top 20 m of borehole AT1 contained materials with higher resistivity. In contrast, the residual of core AT1 was composed of materials with lower resistivity. Therefore, in our model, the higher resistivity materials are likely the original coarser sediments, while the lower resistivity materials are probably the intrusive finer sediments of mud from the deep.

Sediment originated from a deep mud layer and underwent stress-induced compression

Particle grain size analyses and porosity measurements were conducted on core samples from boreholes AT1 and BH3 (Supplementary Table S1). As shown in Fig. 5 and Supplementary Fig. S1, the grain size of all core samples was smaller than 500 µm. In the upper part of the two cores (less than 20 m), the sediments consisted of particles ranging in size from clay to fine sand, with a mean size of 92 ± 45 µm (45–258 µm), implying a mixture of clay and coarser sediments. In contrast, below a depth of 20 m in core AT1, the particle size was more homogeneous, ranging from clay to silt, with a mean size of 47 ± 4 µm (41–57 µm). In the core AT1, the particle size of the sediments tends to gradually increase from deep to shallow.

In this study, we collected endmember sediments from three distinct strata units to trace the sediment provenance of the boreholes (Fig. 2 and Supplementary Fig. S2): the Holocene deposits (EM1), Liushuang Formation (EM2–4), and Gutingkeng Formation (EM5–8). Those specimens were sampled from outcrops located in the western foothills. The particles also displayed distinct sizes among the endmembers: the Holocene sediments and the Liushuang Formation primarily consist of sand, while the Gutingkeng Formation is mud. According to earlier investigation[35], the shallow zone of our study area is covered by Holocene deposits and the Liushuang Formation, with the Gutingkeng Formation lying beneath these layers at a depth of at least 3 km from the surface (Fig. 2). Compared to sediments from the endmember sites, the particle size for core specimens was similar to that of the Gutingkeng Formation and much smaller than the sediments of the Holocene deposits and the Liushuang Formation. From the perspective of particle size, the Gutingkeng Formation is likely the potential source for the lower part of borehole AT1. Consequently, the indication that the sediments in the AT1 core

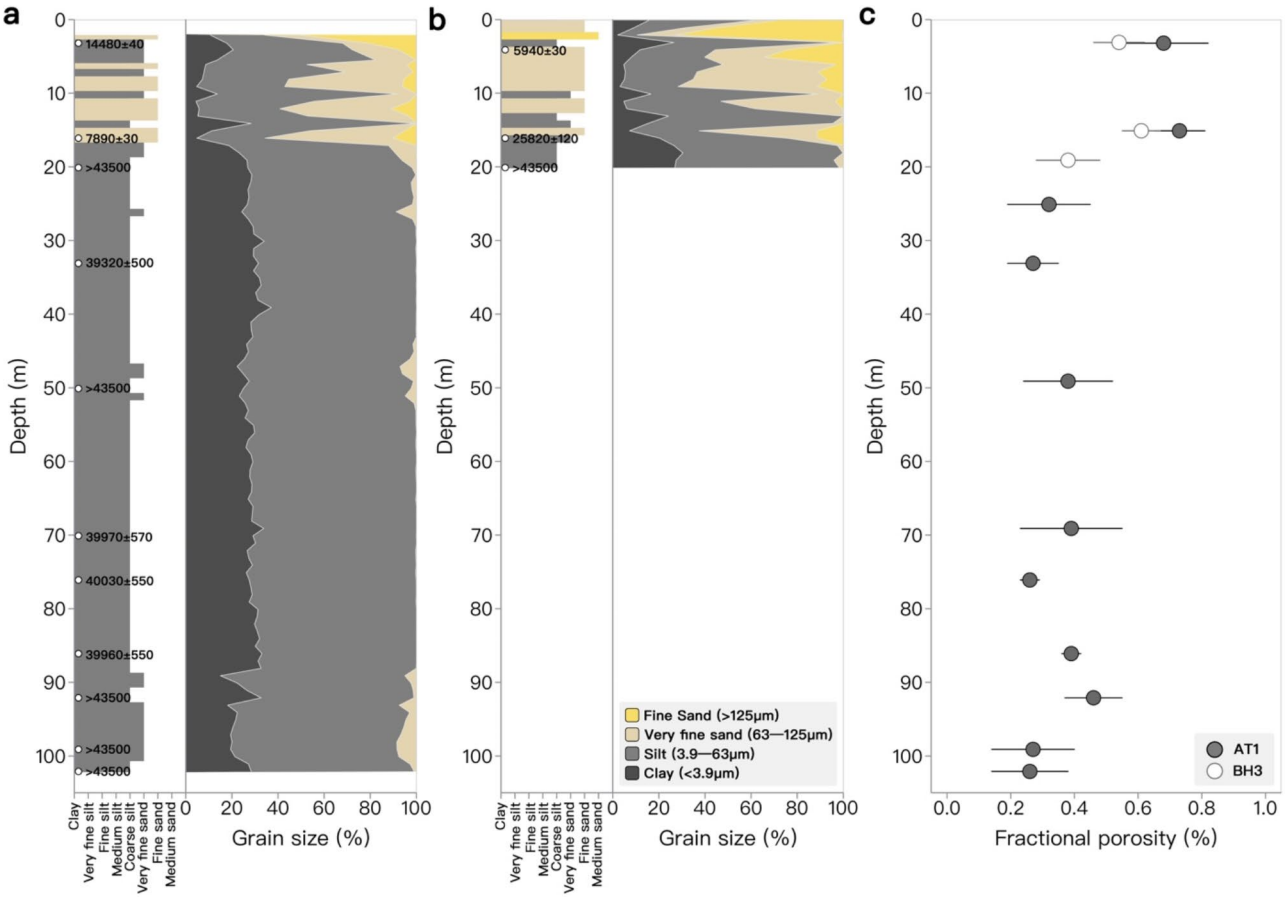

Fig. 5. Downcore distributions of particle grain size and fractional porosity for boreholes. (**a**) Core AT1, (**b**) Core BH3. The numbers represent the C-14 dating ages, indicated as "before present" (BP). (**c**) The fractional porosity represents the mean value measured in the core Sect. (1 m) with a resolution of 1 mm, while the error bars depict the 1σ range of data distributions.

originated from mudstone situated at least 3 km beneath the surface holds considerable significance, further emphasizing the necessity for multidisciplinary evidence.

Carbon-14 dating (Fig. 5a, b) reveals that sediments within the upper 20 m are relatively young, dating from 5940 to 25,820 years before present. In core AT1, sediments found at depths between 20 and 102 m are dated to approximately 40,000 years before present, which aligns with the Pleistocene. In the top 20 m of cores AT1 and BH3, there is notable variability in both particle size and dating results, whereas in the lower 80 m of core AT1, these results exhibit greater consistency. Therefore, it is reasonable to posit that the lower 80 m of the core sediment have a similar source. The depositional age of the Gutingkeng Formation is typically considered to be between the Pleistocene and Eocene[36]. Thus, the core dating result of only 40,000 years suggests that these sediments likely come from the very upper layers of the Gutingkeng Formation.

Figure 5c illustrates the porosity of boreholes AT1 and BH3, revealing that the porosity in the upper 20 m (AT1: 0.71% ± 0.04% and BH3: 0.5% ± 0.1%) is significantly greater than that in the lower section of core AT1 (0.33 ± 0.07%). Several factors influence sediment porosity, including grain size, shape, sorting, and compaction[37,38], which determine the amount and connectivity of pore spaces within the sediments. Since the grain size of our samples was all smaller than fine sand, the effects of sorting and shape are considered relatively negligible. In core AT1, the particle size varies by a factor of about 4.5. Empirical estimations[38] suggest that this could lead to a change in porosity of less 1.5 times. However, the actual porosity variation in the core is up to 2.8 times. Thus, changes in particle size alone cannot fully explain the observed variations. Instead, the significantly lower porosity, particularly in the core's lower section, is most likely due to sediment compaction from compression. This observation is supported by the identification of a shearing zone at depths of 81.3–81.5 m in the core (Supplementary Fig. S3), the strata on either side of the shear zone remain unaltered and exhibit no significant differences in mudstone composition. This feature is interpreted as being formed by horizontal tectonic compaction associated with mud uplift intrusions. This shearing zone is also often accompanied by mud intrusion at its edges, developing together in regions where other mud structures are present[22]. Consequently, based on the above physical properties, the upper section of core AT1 resembles that of BH3, which represents the original and undisturbed strata. This similarity occurs because borehole BH3 was not drilled in the surface-deformed hotspot area. In contrast, we propose that the fine sediment found in the lower section of core AT1

likely originates from a mud layer located more than 3 km deep. Additionally, this sediment has undergone stress-induced compression.

A mixture of original sediments and deep mud

To confirm the sediment source of borehole AT1, we conducted chemical and isotopic analyses on the core sediments and their potential endmembers (Fig. 6 and Supplementary Table S1). Based on our mineralogical analyses (Supplementary Table S2), quartz, muscovite, clinochlore, and albite were identified as the major mineral phases in these sediments. The key distinction is the presence of calcite in the sediments of the Gutingkeng Formation (EM5–6: 1.7–3.4%) and within the interlayer mud of the Liushuang Formation (EM3-M2–M3: 2.1–4.1%). Thus, the presence of calcite in the mud material potentially led to higher Ca/Na and Mg/Na molar ratios. As a result, these metal-to-Na ratios can be used to distinguish between the sediment sources of the Holocene deposits/Liushuang Formation and the Gutingkeng Formation. Figure 6a shows a clear pattern indicating two different sources: sand with lower values and mud with higher values. Most of the core specimens exhibited Ca/Na ratios similar to those of the mud, while the Mg/Na ratios fell between the two endmembers. Notably, sample BH3-16 contained plentiful calcites, resulting in a remarkedly higher metal/Na ratio. These results imply that the core sediment is primarily composed of mud with a minor amount of sand. It is likely that, during the upward movement of the deep mud, a large amount of the original, relatively coarser-grained sediment was replaced.

Neodymium isotopes serve as robust and sensitive tracers for sediment provenance[29,39–41]. Figure 6b unveiled less radiogenic εNd (refer to Eq. 1 in Methods) for the older mud of the Gutingkeng Formation and relatively more radiogenic for the younger sand of the Liushuang Formation. The Holocene sediments (EM1) exhibit significantly distinct εNd values compared to other source endmembers. A binary mixing model of mud (EM5–8) and sand (EM2–4) was created using a Monte-Carlo approach with 100,000 iterations, accounting for the mean and standard deviation (1σ) of the endmembers. Except for the top layers, the core specimens fell within the binary mixing region, indicating a mixture of mud and original deposits. This argument is further supported by the correlation between particle grain size and sediment εNd compositions (Fig. 6c). Therefore, we argue that when the mean grain size of the core sediment exceeds 15 μm, it reflects the original deposits. Conversely, if the grain size is less than 15 μm, it suggests replacement by mud. Samples from a depth of 70 m deviated from this pattern, likely due to mixing with sediments from other sources. Further analysis is needed to clarify this.

Sediment provenance revealed by synchrotron X-ray absorption

In addition to geochemical approaches, we further employed spectroscopy analysis using synchrotron radiation to trace the sediment sources and validate our model. An XAS study has been conducted to reveal the electronic structure around the absorbing atom Fe, which can be characterized by features around the absorption edge, called X-ray absorption near-edge structure (XANES). It is believed that XANES can serve as a fingerprint to provide information about structural descriptors, including crystal structure, type of neighboring atom, and oxidation and chemical state, by affecting the spectral descriptors such as edge position and shapes and positions of spectral maxima and minima[42,43] of the iron species in studied materials. Since the mudstone of the Gutingkeng Formation was deposited in reducing deep-sea environments[18,44], while the sandstone of the Liushuang Formation and the Holocene sediments were formed under more oxidizing conditions, significant differences in the redox states of these sedimentary environments likely lead to variations in the formation of iron oxide compounds. Figure 7a shows the K-edge absorption spectra of iron oxides for the endmember specimens, highlighting notable variations in absorption energies: the highest for the Holocene sediment, followed by the Liushuang Formation, and the lowest for the Gutingkeng Formation. The shifts in absorption energy generally reflect changes in the valence state of iron. Therefore, the first-order derivative of the spectra (Fig. 7b) suggests higher proportions of oxidized iron in the sediments of the Holocene and Liushuang sediments, whereas reduced iron states dominate in the sediments of the Gutingkeng Formation. Hence, examining the oxidation states of iron in sediments allows for an effective reconstruction of the redox conditions in the sedimentary environment, which can be further used to determine sediment provenance.

Figure 7c displays the iron K-edge absorption spectra for the AT1 core specimens. Our results revealed consistent patterns for samples below a depth of 20 m, with only the shallow specimens showing differences. The first-order derivative of the spectra (Fig. 7d) suggests that the valence state of iron in those core specimens closely resembles that of the Gutingkeng Formation, implying that the mudstone is the primary source of the core sediment. However, slight differences in the spectra were observed between them, suggesting that the sediment from the Gutingkeng Formation does not entirely dominate the core sediment. Linear combination fitting analyses show that the maximum similarity between the spectra of core specimens and the mud endmember is only 90%, implying that the sediment is a mixture of at least two sources. Additionally, the fitting similarity significantly decreases in the surface sediment of the core. Therefore, based on both geochemical and physical evidence, the core sediment primarily originates from deep mud and is mixed with the original deposits, specifically the sand from the Liushuang Formation.

Implications on surface deformation and fault developments in orogenic regimes

Overall, this study is the first to present evidence of mud diatreme in the orogenic region of SW Taiwan from multiple disciplinary perspectives. The findings suggest that these mud diapiric intrusions create a series of structural highs beneath the surface, shaping the landform[18]. The formation of these structures is primarily attributed to overpressure in sedimentary layers[45,46], compressional tectonic forces, and gas-bearing fluids[18,22,47]. This phenomenon is likely to occur in tectonically collisional areas, such as the off- and on-shore southern Taiwan[16,48–51], the northern South China Sea[52,53], the Nankai Trough[54,55], the Andaman Sea Basin[56], the Mediterranean regions[57–59], the onshore Caribbean region of Colombia[60,61], the Gulf of Cádiz[62,63], and Ireland[64], as well as in extensional settings like the Black Sea[62,65] and the Southeastern Tyrrhenian Sea[66,67]. As a result, mud

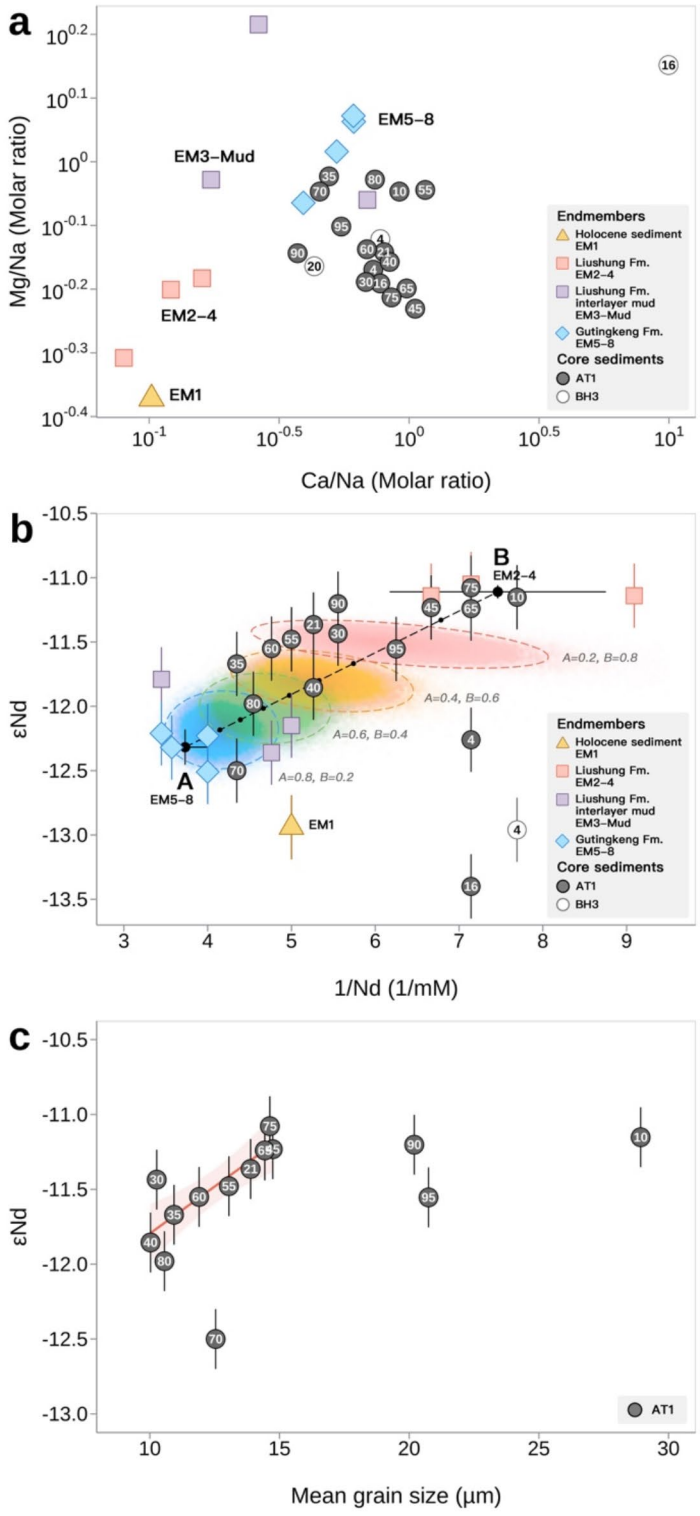

Fig. 6. Elemental and εNd compositions for the boreholes and endmember specimens. (**a**) metal-to-Na ratios, (**b**) εNd and Nd concentration, and (**c**) the correlation between core AT1 sediment grain size and εNd compositions. In (**b**), A and B represented the mean and 1σ data distributions for the Gutingkeng Fm. Mud (EM 5–8) and Liushung Fm. Sand (EM 2–4), respectively. A Monte-Carlo simulation showcasing binary mixing across various relative proportions of endmembers A and B. The error bars in (**b**) and (**c**) indicate the long-term reproducibility of εNd determinations. The numbers in the core sediment present the depths of the boreholes in meters.

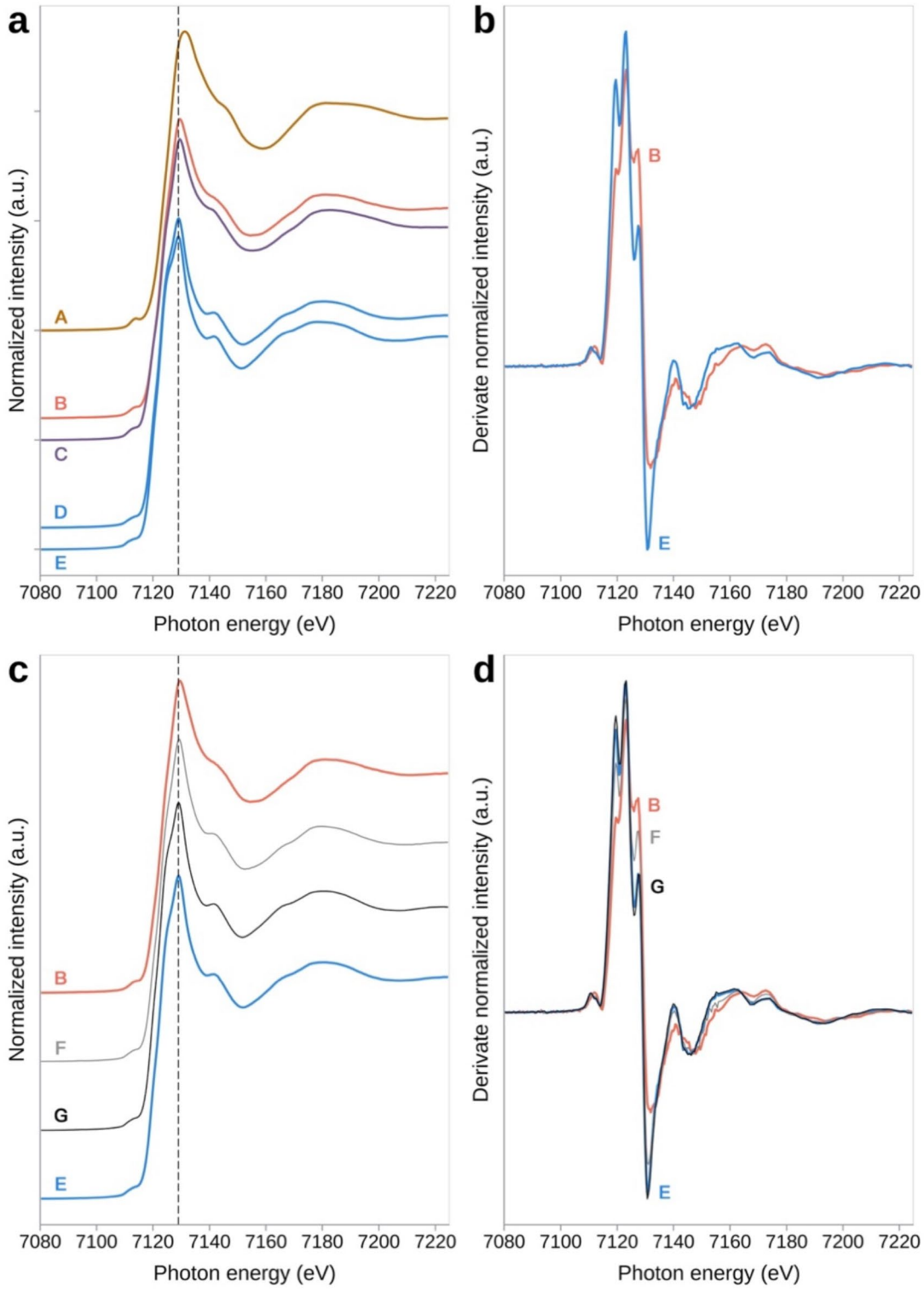

Fig. 7. The K-edge spectra for the endmember and core AT1 specimens. (**a**,**b**) The normalized intensity and its derivative spectrum for the endmember specimens, including the Holocene sediment (A: EM1), Liushung Formation sand (B: EM3), the interlayered mud in EM3 (C), and Gutingkeng Formation mud (D: EM5 and E: EM8). (**c**,**d**) A comparison of the normalized intensity and its derivative spectrum for the core AT1 specimens (F: core top at a depth of 4 m and G: core bottom at a depth of 80 m) and the endmember specimens.

Data availability.

intrusive structures and their geological impacts are potentially widespread globally, occurring both onshore and offshore.

Mud intrusions not only cause surface deformation but may also be accompanied by fault development[20,51]. Mud intrusions are influenced by both lateral compressive stress and vertical uplift stress, with fault patterns depending on the principal stress direction. When lateral compressive stress is the main driver, thrust faults can develop alongside the intrusions (Fault I in Fig. 3). Different compressive stresses result in various thrust and back-thrust faults[68]. If uplift is primarily due to overpressure and buoyancy, normal faults form within the mud intrusions[69] (Fault II and III in Fig. 3). Additionally, dominant lateral compressive stress can reverse these normal faults into high-angle thrust faults. Most mud intrusions in the SW offshore region of Taiwan are attributed to vertical uplift stress, resulting in the development of a series of normal faults[18]. Mud diapirs in offshore areas are generally believed to extend laterally to land, including the region of this study. The faults discovered around the Tainan Anticline (Fold A in Fig. 2), whether defined as normal faults[11,70] or thrust faults[71], are related to the mud intrusions[14]. Consequently, the anomalous geophysical properties of mud diatremes, including low porosity, low strength, and high compactness, create a conducive environment for the development of nearby fault systems.

Our ERT image (Fig. 4) reveals that the point-scatter and irregular distribution of mud diatremes can cause localized uneven uplift, potentially damaging structures and building foundations. This suggests that the massive mud intrusion, or mud diapir, likely only extends to a shallow depth below the surface, while the induced fractures act as conduits that reach the ground surface (Fig. 3b). This study indicates that surface deformation caused by mud intrusions manifests as numerous small-scale hotspots. Electrical resistivity measurements are an economical and efficient exploration method, enabling construction projects to avoid critical deformation hotspots. Additionally, even if construction cannot avoid these hotspots, the slow rate of deformation suggests that reinforced construction techniques should effectively address the issues. Effective exploration and appropriate construction methods aim to prevent surface deformation caused by mud intrusions, enhance the resilience of buildings against associated fault activities, and improve urban safety by mitigating related geological hazards.

Conclusion

The intrusion of deep mud appears to cause localized uplift and deformation at the surface, often accompanied by fault activity. For instance, thrust faults may form under compressive stress, while high-angle normal faults may develop due to overpressure and buoyancy. These hazards can pose significant engineering and geological risks. In SW Taiwan, upward migration of mud from deep underground is quite common. While mud diapirs were previously suggested as an explanation for surface deformation, they fail to adequately account for the widespread, sporadic pattern of uplift and building damage observed.

This study presents compelling evidence through a combination of geophysical, geochemical, and synchrotron-based analyses. These analyses reveal that fine-grained mud from deep strata (the Gutingkeng Formation, located at least 3 km below the surface) has intruded upward and mixed with overlying, coarser-grained sediments in SW Taiwan. ERT imaging identified zones of low resistivity extending to depths of approximately 100 m. The low resistivity zones were confirmed by drilling and laboratory analyses, which revealed the presence of fine, compacted sediments distinct from the near-surface Holocene and Liushuang Formations. Geochemical tracers, such as metal/Na ratios and Nd isotopes, and iron oxidation-state fingerprints obtained through XANES, further support the origin of much of the sediment in the deeper sections of borehole AT1 from the Gutingkeng Formation. Based on the AT1 core with a boundary set at 20 m depth, the differences in particle size, porosity, and Nd isotopes between the upper and lower sediments suggest distinct sediment sources. These sources also correspond to the resistivity variations observed in the ERT image. Therefore, the ERT results indicate that the low-resistivity zone extending from the surface to below 100 m is highly probable to be an area where mudstone has intruded. Consequently, in the ERT images, the low-resistivity zones that extend into deeper formations potentially indicate mud intrusion. This makes ERT imaging both an efficient and cost-effective tool for rapidly scanning underground structures to assess potential mud intrusion areas, thereby reducing safety concerns and risks associated with geological hazards. Furthermore, the ERT results reveal sporadic (rather than large-scale) low-resistivity hotspots on the near-surface in the area of positive residual gravity anomalies. This finding demonstrates that the actual causes of surface uplift and building damage are the extension of fractures leading to surface deformation, namely the phenomenon of mud diatremes.

Data availability

The datasets used and/or analyzed during the current study are included in its supplementary information files and are also available from the corresponding author upon reasonable request.

Received: 11 July 2024; Accepted: 24 February 2025
Published online: 05 March 2025

References

1. Cole, G. L., Dhakal, R. P. & Turner, F. M. Building pounding damage observed in the 2011 Christchurch earthquake. *Earthq. Eng. Struct. Dyn.* **41**, 893–913 (2012).
2. Anderson, J. G. & Hough, S. E. A model for the shape of the fourier amplitude spectrum of acceleration at high frequencies. *Bull. Seismol. Soc. Am.* **74**, 1969–1993 (1984).
3. Singh, S. K. et al. The Mexico earthquake of September 19, 1985—A study of amplification of seismic waves in the Valley of Mexico with respect to a hill zone site. *Earthq. Spectra* **4**, 653–673 (1988).
4. Wells, D. L. & Coppersmith, K. J. New empirical relationships among magnitude, rupture length, rupture width, rupture area, and surface displacement. *Bull. Seismol. Soc. Am.* **84**, 974–1002 (1994).
5. Stein, R. S. & Yeats, R. S. Hidden earthquakes. *Sci. Am.* **260**, 48–57 (1989).

6. Akkar, S. & Bommer, J. J. Empirical prediction equations for peak ground velocity derived from strong-motion records from Europe and the middle East. *Bull. Seismol. Soc. Am.* **97**, 511–530 (2007).
7. Makris, N. & Gazetas, G. Dynamic pile-soil-pile interaction. Part II: lateral and seismic response. *Earthq. Eng. Struct. Dyn.* **21**, 145–162 (1992).
8. Schwartz, D. P. & Coppersmith, K. J. Fault behavior and characteristic earthquakes: examples from the Wasatch and San Andreas fault zones. *J. Geophys. Res. Solid Earth*. **89**, 5681–5698 (1984).
9. Chen, S. C., Ching, K. E., Lo, Y. T. & Lu, W. C. Mud diapiric characters, activities and geohazards of the Tainan and Chungchou anticlines. *Bull. Cent. Geol. Surv. MOEA*. **33**, 1–32 (2020).
10. Hsiao, S. H., Ching, K. E., Chen, K. H. & Li, C. K. Timing of coseismic displacement grid model construction for updating the semi-kinematic reference frame: case study in Taiwan. *J. Geod.* **95**, 25 (2021).
11. Hsieh, S. H. Subsurface geology and gravity anomalies of the Tainan and Chungchou structures of the coastal plain of Southwestern Taiwan. *Pet. Geol. Taiwan.* **10**, 323–338 (1972).
12. Lin, A. T. & Watts, A. B. Origin of the West Taiwan basin by orogenic loading and flexure of a rifted continental margin. *J. Geophys. Res. Solid Earth* 107, ETG 2-1-ETG 2–19 (2002).
13. Ching, K. E., Rau, R. J., Lee, J. C. & Hu, J. C. Contemporary deformation of tectonic escape in SW Taiwan from GPS observations, 1995–2005. *Earth Planet. Sci. Lett.* **262**, 601–619 (2007).
14. Huang, M. H. et al. Active deformation of Tainan tableland of Southwestern Taiwan based on geodetic measurements and SAR interferometry. *Tectonophysics* **466**, 322–334 (2009).
15. Rau, R. J. et al. Surface deformation and earthquake potential of Tainan tableland, Southwestern Taiwan. *Bull. Cent. Geol. Surv. MOEA*. **14**, 161–171 (2003).
16. Lo, Y. T., Ching, K. E., Yen, H. Y. & Chen, S. C. Bouguer gravity anomalies and the three-dimensional density structure of a Thick mudstone area: A case study of Southwestern Taiwan. *Tectonophysics* **848**, 229730 (2023).
17. Kopf, A. J. Significance of mud volcanism. *Rev. Geophys.* 40, 2-1-2–52 (2002).
18. Chen, S. C. et al. Distribution and characters of the mud diapirs and mud volcanoes off Southwest Taiwan. *J. Asian Earth Sci.* **92**, 201–214 (2014).
19. Huang, S. T. et al. Deformation front development at the Northeast margin of the Tainan basin, Tainan–Kaohsiung area, Taiwan. *Mar. Geophys. Res.* **25**, 139–156 (2004).
20. Wang, Y. et al. Mud diapir or fault-related fold? On the development of an active mud-cored anticline offshore Southwestern Taiwan. *Tectonics* **41** (2022).
21. Lin, G. P. *Crustal Deformation of Tainan Region from Persistent Scatterer Interferometry* (National Central University, 2012).
22. Brown, K. M. The nature and hydrogeologic significance of mud diapirs and diatremes for accretionary systems. *J. Geophys. Res. Solid Earth*. **95**, 8969–8982 (1990).
23. Ching, K. E. et al. Rapid deformation rates due to development of diapiric anticline in Southwestern Taiwan from geodetic observations. *Tectonophysics* **692**, 241–251 (2016).
24. Tsai, W. N. et al. Electrical resistivity tomography (ERT) monitoring for landslides: case study in the Lantai area, Yilan Taiping mountain, Northeast Taiwan. *Front. Earth Sci.* **9**, 737271 (2021).
25. Zhang, G. et al. Imaging rainfall infiltration processes with the time-lapse electrical resistivity imaging method. *Pure Appl. Geophys.* **173**, 2227–2239 (2016).
26. Yu, P. S. & Chen, T. T. An integrated, non-destructive method for evaluating core quality from R/V Legend's giant piston coring system (LGD-GPC). *Terr. Atmos. Ocean. Sci.* **34**, 17 (2023).
27. Reimer, P. J. et al. The IntCal20 Northern hemisphere radiocarbon age calibration curve (0–55 cal kBP). *Radiocarbon* **62**, 725–757 (2020).
28. Ravel, B. & Newville, M. A. T. H. E. N. A. ARTEMIS, HEPHAESTUS: data analysis for X-ray absorption spectroscopy using IFEFFIT. *J. Synchrotron Radiat.* **12**, 537–541 (2005).
29. Huang, K. F., You, C. F., Chung, C. H., Lin, Y. H. & Liu, Z. Tracing the Nd isotope evolution of North Pacific intermediate and deep waters through the last deglaciation from South China sea sediments. *J. Asian Earth Sci.* **79**, 564–573 (2014).
30. Jacobsen, S. B. & Wasserburg, G. J. Sm-Nd isotopic evolution of chondrites. *Earth Planet. Sci. Lett.* **50**, 139–155 (1980).
31. Fuenlabrada, J. M. High-precision Sr and Nd isotope characterization of BHVO-2 reference material by thermal ionization mass spectrometry. *Rapid Commun. Mass Spectrom.* **37**, e9632 (2023).
32. Raczek, I., Jochum, K. P. & Hofmann, A. W. Neodymium and strontium isotope data for USGS reference materials BCR-1, BCR-2, BHVO-1, BHVO-2, AGV-1, AGV-2, GSP-1, GSP-2 and eight MPI-DING reference glasses. *Geostand Newsl.* **27**, 173–179 (2003).
33. Luu, T. H., Gutiérrez, P., Inglis, E. C., Roberts, D. & Chauvel, C. High-precision Sr and Nd isotope measurements using a dynamic zoom lens-equipped thermal ionisation mass spectrometer. *Chem. Geol.* **611**, 121078 (2022).
34. Saji, N. S., Wielandt, D., Paton, C. & Bizzarro, M. Ultra-high-precision Nd-isotope measurements of geological materials by MC-ICPMS. *J. Anal. Spectrom.* **31**, 1490–1504 (2016).
35. Chen, W. S., Huang, N. W. & Yang, C. C. Pleistocene sequence stratigraphic characteristics and foreland basin evolution, Southwestern Taiwan. *Spec. Publ Cent. Geol. Surv. MOEA*. **25**, 1–38 (2011).
36. Nagel, S. et al. Sedimentology and foreland basin paleogeography during Taiwan Arc continent collision. *J. Asian Earth Sci.* **62**, 180–204 (2013).
37. Yang, Y. & Aplin, A. C. Permeability and petrophysical properties of 30 natural mudstones. *J. Geophys. Res. Solid Earth* **112**, (2007).
38. Wilson, R. J., Speirs, D. C., Sabatino, A. & Heath, M. R. A synthetic map of the north-west European shelf sedimentary environment for applications in marine science. *Earth Syst. Sci. Data* **10**, 109–130 (2017).
39. You, C. F., Liao, W. L., Huang, K. F., Chung, C. H. & Liu, Z. Sediment source variation using REEs, Sr, and Nd isotopic compositions: a case study in MD05-2901, Northwestern South China sea. *Front. Mar. Sci.* **10**, 1292802 (2024).
40. Mantovanelli, S. S., Tassinari, C. C. G., Mahiques, M. M. D., Jovane, L. & Bongiolo, E. Characterization of Nd radiogenic isotope signatures in sediments from the Southwestern Atlantic margin. *Front. Earth Sci.* **6**, 74 (2018).
41. Liu, Z. et al. Source-to-sink transport processes of fluvial sediments in the South China sea. *Earth Sci. Rev.* **153**, 238–273 (2016).
42. Wilke, M., Farges, F., Petit, P. E., Brown, G. E. & Martin, F. Oxidation state and coordination of Fe in minerals: an Fe K-XANES spectroscopic study. *Am. Min.* **86**, 714–730 (2001).
43. Liu, J. et al. Altered chemistry of oxygen and iron under deep Earth conditions. *Nat. Commun.* **10**, 153 (2019).
44. Chang, K. H. *Evolution of Sedimentary Environments in Initial Stage of Foreland Basin Southwest Taiwan* (National Cheng Kung University, 2015).
45. Milkov, A. V. Worldwide distribution of submarine mud volcanoes and associated gas hydrates. *Mar. Geol.* **167**, 29–42 (2000).
46. Talukder, A. R. et al. High-resolution, deep tow, multichannel seismic and sidescan sonar survey of the submarine mounds and associated BSR off Nicaragua Pacific margin. *Mar. Geol.* **241**, 33–43 (2007).
47. Hovland, M. & Curzi, P. V. Gas seepage and assumed mud diapirism in the Italian central Adriatic sea. *Mar. Pet. Geol.* **6**, 161–169 (1989).
48. Lin, G. P., Chang, W. L. & Chiu, C. Y. Unraveling the role played by a buried mud diapir: alternative model for 2016 Mw 6.4 MeiNong earthquake in Southwestern Taiwan. *Geosci. Lett.* **11**, 21 (2024).
49. Tan, P., Ding, W. & Li, J. Exhumation history of the Hengchun ridge and its implications for Taiwan orogenic processes. *Front. Earth Sci.* **10**, 941040 (2022).

50. Mai, H. A., Lee, J. C., Chen, K. H. & Wen, K. L. Coulomb stress changes triggering surface pop-up during the 2016 Mw 6.4 Meinong earthquake with implications for earthquake-induced mud diapiring in SW Taiwan. *J. Asian Earth Sci.* **218**, 104847 (2021).
51. Yan, Y. S. et al. Faults caused by the fault: microstructural and mineral characterization of deformation in Chungliao tunnel, Taiwan, caused by Chishan fault. *Eng. Geol.* **292**, 106245 (2021).
52. Yu, J., Yan, P., Wang, Y., Zhong, G. & Chen, C. Subsurface structures and nature of seafloor mounds in the Northern South China sea margin: implications for mesozoic hydrocarbon exploration. *Geomorphology* **445**, 108973 (2024).
53. Zhong, S., Zhang, J., Luo, J., Yuan, Y. & Su, P. Geological characteristics of mud volcanoes and diapirs in the Northern continental margin of the South China Sea: implications for the mechanisms controlling the genesis of fluid leakage structures. *Geofluids* **2021**, 1–17 (2021).
54. Kobayashi, K. et al. Deep-tow survey in the KAIKO-Nankai cold seepage areas. *Earth Planet. Sci. Lett.* **109**, 347–354 (1992).
55. Asada, M., Moore, G. F., Kawamura, K. & Noguchi, T. Mud volcano possibly linked to seismogenic faults in the Kumano basin, Nankai trough, Japan. *Mar. Geophys. Res.* **42**, 4 (2021).
56. He, W. & Zhou, J. Structural features and formation conditions of mud diapirs in the Andaman sea basin. *Geol. Mag.* **156**, 659–668 (2019).
57. Limonov, A. F., Woodside, J. M., Cita, M. B. & Ivanov, M. K. The mediterranean ridge and related mud diapirism: a background. *Mar. Geol.* **132**, 7–19 (1996).
58. Camerlenghi, A. et al. Geophysical evidence of mud diapirism on the mediterranean ridge accretionary complex. *Mar. Geophys. Res.* **17**, 115–141 (1995).
59. Kopf, A., Robertson, A. H. F. & Volkmann, N. Origin of mud breccia from the mediterranean ridge accretionary complex based on evidence of the maturity of organic matter and related petrographic and regional tectonic evidence. *Mar. Geol.* **166**, 65–82 (2000).
60. Trejos-Tamayo, R. et al. Biostratigraphy of ejected material from mud volcanoes in the Caribbean region of Colombia: contribution to the stratigraphy of Sinú basin. *J. S Am. Earth Sci.* **103**, 102782 (2020).
61. Dill, H. G., Ufer, K., Bornemann, A., Techmer, A. & Buzatu, A. From the strand plain to the reef: A sedimentological–geomorphological study of a holocene Coast affected by mud diapirism (Archipélago Rosario- Barú, Colombia). *Mar. Geol.* **415**, 105953 (2019).
62. Somoza, L. et al. Seabed morphology and hydrocarbon seepage in the Gulf of Cádiz mud volcano area: acoustic imagery, multibeam and ultra-high resolution seismic data. *Mar. Geol.* **195**, 153–176 (2003).
63. Palomino, D. et al. Multidisciplinary study of mud volcanoes and diapirs and their relationship to seepages and bottom currents in the Gulf of Cádiz continental slope (northeastern sector). *Mar. Geol.* **378**, 196–212 (2016).
64. Blanchard, S. et al. Early burial mud diapirism and its impact on stratigraphic architecture in the carboniferous of the Shannon basin, County Clare. *Irel. Sedimentology* **66**, 329–361 (2019).
65. Krastel, S. et al. Acoustic investigations of mud volcanoes in the Sorokin trough, black sea. *Geo-Mar. Lett.* **23**, 230–238 (2003).
66. Gamberi, F. & Rovere, M. Mud diapirs, mud volcanoes and fluid flow in the Rear of the Calabrian Arc orogenic wedge (southeastern tyrrhenian sea). *Basin Res.* **22**, 452–464 (2010).
67. Rovere, M. et al. Venting and seepage systems associated with mud volcanoes and mud diapirs in the Southern tyrrhenian sea. *Mar. Geol.* **347**, 153–171 (2014).
68. Dooley, T. P., Jackson, M. P. A. & Hudec, M. R. Inflation and deflation of deeply buried salt stocks during lateral shortening. *J. Struct. Geol.* **31**, 582–600 (2009).
69. Tvedt, A. B. M., Rotevatn, A. & Jackson, C. A. L. Supra-salt normal fault growth during the rise and fall of a diapir: perspectives from 3D seismic reflection data, Norwegian North sea. *J. Struct. Geol.* **91**, 1–26 (2016).
70. Chen, Y. G. & Liu, T. K. Holocene uplift and subsidence along an active tectonic margin Southwestern Taiwan. *Quatern Sci. Rev.* **19**, 923–930 (2000).
71. Béon, M. L. et al. Shallow geological structures triggered during the Mw 6.4 Meinong earthquake, Southwestern Taiwan. *Terr. Atmos. Ocean. Sci.* **28**, 663–681 (2017).
72. Pérez-Belzuz, F., Alonso, B. & Ercilla, G. History of mud diapirism and trigger mechanisms in the Western Alboran sea. *Tectonophysics* **282**, 399–422 (1997).

Acknowledgements

This research was supported in part by Higher Education Sprout Project, Ministry of Education to the Headquarters of University Advancement at National Cheng Kung University (NCKU). This work was partly supported by grants from the National Science and Technology Council Taiwan to H.-C. Liu (NSTC 112-2636-M-006-011-), H.-Y. Wu (NSTC 112-2116-M-006-006-) and C.-C. Chen (NSTC 112-2740-M-008-005-). The authors acknowledge the two anonymous reviewers for their invaluable comments and suggestions on this study and the editor for handling this manuscript.

Author contributions

K.-E. Ching, H.-C. Liu, H.-Y. Wu, and L.-C. Kao conceptualized the research framework and defined the primary objectives of this study. H.-Y. Wu, H.-C. Liu, L.-C. Kao, C.-C. Chen, and K.-E. Ching co-wrote and thoroughly managed this paper. T.-C. Yi, Y.-H. Chen, and H.-Y. Wu performed the sampling. C.-C. Chen carried out the ERT analyses. H.-Y. Wu and B.-L. Wu conducted the sediment core analyses. Y.-H. Chen handled the chemical and isotopic data analyses with instrumental support from C.-F. You. L.-C. Kao performed the synchrotron analyses. C.-J. Chen conducted the XRD analyses. H.-C. Liu, H.-Y. Wu, C.-F. You, and K.-E. Ching contributed to the data discussion and validation.

Declarations

Competing interests

The authors declare no competing interests.

Additional information

Supplementary Information The online version contains supplementary material available at https://doi.org/10.1038/s41598-025-91915-y.

Correspondence and requests for materials should be addressed to H.-C.L.